



ZnS/MMT nanocomposites: The effect of ZnS loading in MMT on the photocatalytic reduction of carbon dioxide



Kamila Kočí^{a,*}, Lenka Matějová^a, Ondřej Kozák^b, Libor Čapek^c, Václav Valeš^d,
Martin Reli^a, Petr Praus^a, Klára Šafářová^b, Andrzej Kotarba^e, Lucie Obalová^a

^a VŠB-Technical University of Ostrava, 17 listopadu 15, 708 33 Ostrava-Poruba, Czech Republic

^b Regional Centre of Advanced Technologies and Materials, Palacky University, Faculty of Science, Department of Physical Chemistry, 17 listopadu 12, 771 46 Olomouc, Czech Republic

^c University of Pardubice, Faculty of Chemical Technology, Department of Physical Chemistry, Studentská 95, 532 10 Pardubice, Czech Republic

^d Charles University in Prague, Faculty of Mathematics and Physics, Department of Condensed Matter Physics, Ke Karlovu 5, 121 16 Prague 2, Czech Republic

^e Faculty of Chemistry, Jagiellonian University, Ingardena 3, 30-060, Krakow, Poland

ARTICLE INFO

Article history:

Received 18 February 2014

Received in revised form 18 April 2014

Accepted 25 April 2014

Available online 4 May 2014

Keywords:

ZnS nanoparticles

Montmorillonite (MMT)

Nanocomposite

Photocatalysis

Work function

ABSTRACT

Different weight loadings (2–4.2 wt.%) of ZnS nanoparticles stabilized by cetyltrimethylammonium bromide (CTAB) were deposited on montmorillonite (MMT) in order to investigate the performance of ZnS/MMT nanocomposites in the CO₂ photocatalytic reduction. Physicochemical properties of prepared nanocomposites were comprehensively characterized by using nitrogen physisorption, XRD, TEM, DR UV–vis spectroscopy and contact potential difference measurements. The main reaction products in a gas phase were hydrogen and methane. According to the blank test the pristine montmorillonite did not possess any photocatalytic performance. The order in photocatalytic performance of individual ZnS/MMT nanocomposites in CO₂ reduction depending on the ZnS loading was following: 3.1 wt.% ZnS > 4.2 wt.% ZnS > 2.0 wt.% ZnS. This trend was explained based on UV–vis, TEM and contact potential difference measurements as follows. The increasing loading of ZnS nanoparticles affects the degree of ZnS nanoparticles agglomeration on MMT and this agglomeration finally influences the properties/behavior within electronic structure of ZnS, correlating with the photocatalytic performance of ZnS/MMT nanocomposites in the CO₂ reduction.

© 2014 Elsevier B.V. All rights reserved.

1. Introduction

Carbon dioxide has increased in the atmosphere from fossil fuel use in industry and transportation, manufacture of cement, building air conditioning and deforestation. With a global radiative forcing of 1.74 W/m², CO₂ is the largest contributor among well-mixed long-lived greenhouse gases, accounting for more than 63% of the total [1]. Although the remediation of CO₂ can be physically stored or chemically transformed, its storage overcomes the problem only temporarily. To solve the CO₂ problem permanently requires the transformation of CO₂ into other valuable and non-toxic compounds. The reduction of CO₂ by photocatalysts is one of the most promising methods [1,2].

Several semiconductors exhibit band gap energies suitable for the photocatalytic reduction of carbon dioxide (for example CdS [3–7], ZrO₂ [8–13], MgO [14,15], ZnO [16], TiO₂ [17–27] and ZnS

[2–6,28,29]). Zinc sulphide is a semiconductor with wide direct band gap energy of about 3.6 eV. It seems to be a very promising material for photocatalysis due to the rapid generation of electron–hole pairs by photoexcitation and highly negative reduction potentials of excited electrons.

In principle, inorganic materials with high specific surface area and chemical stability can be used as a host matrix, e.g. SiO₂, TiO₂, montmorillonite (MMT). Natural porous materials such as zeolites and clay minerals belong among good and cheap supports, moreover, with eco-friendly properties. Montmorillonite, a representative natural clay mineral, possesses a layered structure: two silica tetrahedral sheets and an alumina octahedral sheet. The adsorptive property is an advantage to enforce heterogeneous photoactivity when a semiconductor is immobilized [30–40].

Kun et al. [40] observed an increase of photoactivity in the photooxidation of phenol after deposition of TiO₂ in montmorillonite support. Results of these investigations showed that the porous structure and high specific surface area of montmorillonite were beneficial for photoactivity, via enhancing adsorption, which is the determining step in the heterogeneous photocatalytic reaction.

* Corresponding author. Tel.: +420 597 327 309/+420 596 997 309.

E-mail address: kamila.koci@vsb.cz (K. Kočí).

Therefore, the combining of adsorption and heterogeneous photocatalysis makes the photooxidation more effective for the removal of dye compounds from wastewater [30,32].

The effect of different TiCl_3 :montmorillonite ratios on the photocatalytic activity in degradation of methylene blue in an aqueous solution was investigated by Liu et al. [36]. The nanocomposite with TiO_2 :montmorillonite weight ratio of 0.2:1 showed the highest photocatalytic activity because of its relatively large specific surface area and suitable pore-size distribution.

Zhao et al. [37] dealt with the photocatalytic remediation of γ -hexachlorocyclohexane contaminated soils by using the TiO_2 /montmorillonite composite. Their results indicated that the photocatalytic activity of the composites varied with the content of TiO_2 in the order 30% > 50% > 70% > 10% and the strong adsorption capacity of composites and the quantum size effect may contribute to increased photocatalytic activities.

The sulforhodamine B photodegradation over vanadium-doped TiO_2 /montmorillonite nanocomposites was investigated under visible light irradiation [35]. It was revealed that different Ti/MMT ratios affect significantly the microstructure of nanocomposites and as a consequence their photocatalytic activity.

Tahir et al. [34] studied the performance of MMT-loaded TiO_2 nanocomposites in the reduction of CO_2 with H_2O to hydrocarbon fuels. The effect of parameters such as the MMT loading, $\text{H}_2\text{O}/\text{CO}_2$ feed ratios, and the reaction temperature on the TiO_2 photocatalytic activity was investigated. The MMT loading in TiO_2 enhanced the its performance and markedly increased the CO_2 reduction to C_1 – C_3 hydrocarbon fuels.

Results from Boukhatem et al. [39], who dealt with the synthesis and characterization of CdS–montmorillonite nanocomposites and investigated their photocatalytic activity, showed that the photocatalytic activity of synthesized CdS/MMT nanocomposites was significantly improved compared to that of MMT and pure CdS.

Fatimah et al. [31] investigated the photocatalytic and photochemical degradation of methylene blue over ZnO/montmorillonite. Characterizations showed that the ZnO particles were successfully distributed in the montmorillonite support and ZnO/montmorillonite possesses lower band gap energy. The increased MB adsorption over ZnO/montmorillonite resulted in faster photodegradation.

The aim of this work is to explore the CO_2 photocatalytic reduction process on ZnS/MMT nanocomposites with 2.0, 3.1 and 4.2 wt.% of ZnS and to compare it with commercial TiO_2 Evonic P25. The effect of different ZnS to MMT weight ratios on the CO_2 photocatalytic reduction has not been reported yet. Likewise, the work function of ZnS/MMT nanocomposites has not been investigated. The aim is to reveal the correlations between structural, optical and electronic properties of developed nanocomposites and their photocatalytic performance. The photocatalytic reduction of CO_2 in our experimental arrangement takes place in liquid phase with suspended catalysts at room temperature and atmospheric pressure and the reduction products in gas phase are determined.

2. Experimental

2.1. ZnS/MMT nanocomposites preparation

Two-step preparation of ZnS/MMT was described in detail in our previous work [28]. Briefly, ZnS nanoparticles were formed by adding of the sodium sulphide and cetyltrimethylammonium bromide (CTAB) solution (solution A) dropwise to the solution of zinc acetate (solution B). The ZnS-CTAB was subsequently deposited on montmorillonite by shaking 1 L of 2 mM ZnS solution with 2 g of MMT for 24 h followed by filtration, washing and drying. Two variations in the above-described synthesis were done in order

to positively influence the resulting nanocomposite efficiency. The first one, the addition of the solution B to the solution A changes pH during the ZnS nanoparticles nucleation since sodium sulphide is a base. The composite obtained by shaking such formed ZnS nanoparticles with MMT was denoted as 4.2 wt.% ZnS/MMT. The second variation, the ratio of ZnS suspension volume to MMT weight was varied from 1:2 (L:g) to 1:4 and 1:8, resulting in nanocomposites denoted as 3.1 wt.% ZnS/MMT and 2.0 wt.% ZnS/MMT.

2.2. Characterization of ZnS/MMT nanocomposites

The content of ZnS in ZnS/MMT nanocomposites was determined by elemental analysis of sulphur performed by a combustion analyser ELTRA (Eltra, Germany) and determination of zinc after their dissolution in a mixture of HF, HNO_3 and HClO_4 [41] by an atomic absorption spectrometer AA280FS (Varian Inc., Austria).

The nitrogen adsorption–desorption measurements at 77 K were performed using the volumetric apparatus Nova2000e (Quantachrome, USA). Prior to the nitrogen physisorption measurements, the samples were degassed at 105 °C for 4 h under vacuum less than 1 Pa. Degassing at temperature of 105 °C was applied in order to remove physisorbed water, however, with no influence on the textural or structural properties of investigated nanocomposites. The specific surface area, S_{BET} , was calculated according to the classical Brunauer–Emmett–Teller (BET) theory for the relative pressure range $p/p_0 = 0.05$ – 0.30 [42]. Since the specific surface area, S_{BET} , is not such a proper parameter in the case of mesoporous solids containing some micropores [42,43], the mesopore surface area, S_{meso} , and the micropore volume, V_{micro} , were additionally also evaluated based on the t -plot method [44], using DeBoer standard isotherm. The net pore volume, V_{net} , was determined from the nitrogen adsorption isotherm at maximum p/p_0 (~ 0.991). The mesopore-size distribution (pore diameter 3–130 nm) was evaluated from the adsorption branch of the nitrogen adsorption–desorption isotherm by the Barrett–Joyner–Halenda (BJH) method [45], using the DeBoer standard isotherm and the assumption of the cylindrical pore geometry.

The X-ray diffraction powder (XRD) patterns were measured by a standard laboratory diffractometer in the conventional focusing Bragg–Brentano geometry with variable slits (Ni-filtered $\text{Cu K}\alpha$, 1.4 kW). A linear detector was used to collect the scattered intensity.

Transmission electron microscopy (TEM) observations were carried out on a JEOL 2010F microscope operated at 200 kV (LaB6 cathode, resolution 0.19 nm) using carbon coated copper grid.

UV–vis diffuse reflectance spectra of prepared samples (grain size < 0.160 mm) were measured by using a GBS CINTRA 303 spectrometer equipped with a Spectralon-coated integrating sphere using a Spectralon coated discs as a standard. The spectra were recorded in the range of the wavelength 200–800 nm (lamps switched at 350 nm). The reflectances were re-calculated to the absorption using the Schuster–Kubelka–Munk equation, $F(R_\infty) = (1 - R_\infty)^2 / 2R_\infty$, where R_∞ is the diffuse reflectance from a semi-infinite layer. The obtained spectra were transformed to the dependencies $(F(R_\infty) \cdot h\nu)^2$ against $h\nu$ and assuming that the Tauc's law [46,47] can be expressed as: $(F(R_\infty) \cdot h\nu)^2 \approx (h\nu - E_g)$, where the E_g is the energy of absorption edge values (determined from obtained plots), h is the Planck constant and ν is the light frequency. Kubelka–Munk function was used to estimate the band gap energy of prepared photocatalysts. The optical absorption threshold (\lg) was calculated using the equation, $\lg = 1240/\text{EB}$, where EB is the band gap energy.

The contact potential difference (V_{CPD}) measurements were carried out by the dynamic condenser method of Kelvin with a KP6500 probe (McAllister Technical Services). The reference electrode was a standard stainless steel plate with diameter of 3 mm ($\Phi_{\text{ref}} = 4.3$ eV)

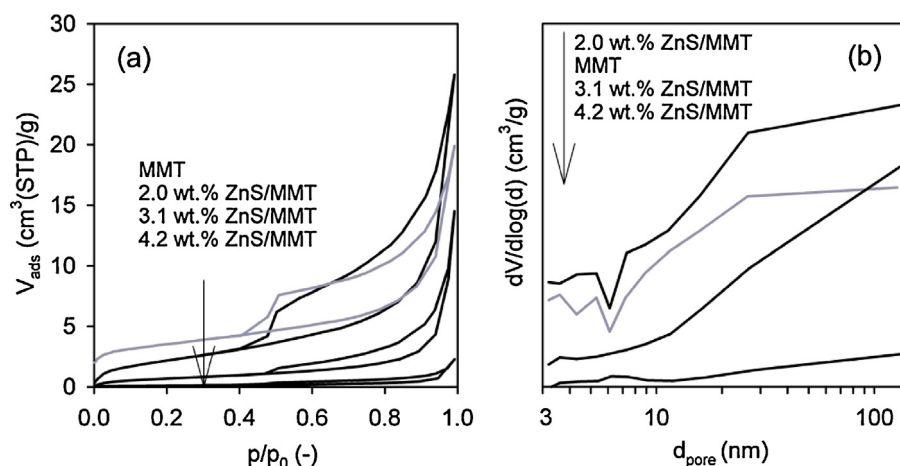


Fig. 1. (a) Measured nitrogen adsorption-desorption isotherms and (b) evaluated pore-size distributions of investigated ZnS/MMT nanocomposites.

provided by the manufacturer. During the measurements the gradient of the peak-to-peak versus backing potential was set to 0.2, whereas the vibration frequency and amplitude was set to 120 Hz and 40 a.u. The final V_{CPD} value was an average of 60 independent points using two backing potentials. The measurements were carried out under atmospheric pressure and ambient temperature. Before measurements the samples were pressed into pellets of 10 mm diameter using the 8 MPa pressure. The work function values were obtained from a simple relation $V_{CPD} = \Phi_{ref} - \Phi_{sample}$.

2.3. Photocatalytic reduction of carbon dioxide

The photocatalytic reduction of carbon dioxide was carried out in a stirred batch annular reactor with a suspended catalyst illuminated by the UV 8 W Hg-lamp (254 nm). The CO_2 diffusion from the gas phase through the gas-liquid interface in a laboratory batch slurry reactor was eliminated by saturating the aqueous solutions of 0.2 mmol/L NaOH with pure CO_2 before the beginning of reactions. During this step, pH decreased from 11.8 to 6.6. The catalyst loading of 1 g/L was chosen to avoid the concentration gradients in a bulk of stirred liquid with the dispersion due to a scattering effect of light as a result of the high nanocomposite concentration. A suitable volume of 100 mL of the liquid phase was used to ensure the perfect mixing in this photoreactor [48]. CO_2 reduction products, such as hydrogen, methane and carbon monoxide, were analysed by a gas chromatograph (GC—Agilent Technologies 6890N) equipped with FID and TCD detectors (GC/FID/TCD) and the Molsieve and HP Poraplot Q columns. The calibration with certified calibration gases (0.05 mol.% CH_4 , 0.987 mol.% H_2 , 2.02 mol.% CO , and 99.999 mol.% CO_2) was performed before each experimental run.

3. Results

3.1. Characterization of ZnS/MMT nanocomposites

Concerning the chemical composition of nanocomposites, the elemental analysis and atomic absorption spectroscopy confirmed that investigated ZnS/MMT nanocomposites contained 4.2 wt.%, 3.1 wt.% and 2.0 wt.% of ZnS. In frame of these analyses some content of carbon in individual nanocomposites was also determined as follows: 25.0 wt.%, 19.4 wt.% and 12.0 wt.%. The source of carbon was the stabilizing cationic surfactant CTAB.

With respect to potential application of developed ZnS/MMT nanocomposites in liquid systems, their stability was explored in our previous works [49,50], via their shaking in water for 24 h. The

dispersions were filtered and the UV-vis absorption spectra of filtrates were recorded. There was not detected any typical absorption edge of ZnS nanoparticles at about 320 nm in absorption spectra which means that the ZnS nanoparticles were firmly attached to MMT likely located in its pores [49]. The stability of ZnS/MMT nanocomposites was also confirmed by the derived mathematical model [50].

Fig. 1a and b shows measured nitrogen adsorption-desorption isotherms and evaluated pore-size distributions of investigated ZnS/MMT nanocomposites. Textural properties are summarized in Table 1. The shapes of nitrogen adsorption-desorption isotherms of all ZnS/MMT nanocomposites correspond to porous materials possessing dominantly larger mesopores/macropores. In addition to that, it is evident from Fig. 1a that pristine MMT possesses besides large mesopores/macropores also a small portion of micropores (pores with diameter < 2 nm, $V_{micro} \sim 2$ mm³ liq/g). According to previous research [51], the missing smallest pores in all ZnS/MMT nanocomposites and decreasing nanocomposite specific surface area can be attributed to a plugging of some part of the MMT porous structure, evidently of micropores and smaller mesopores, by CTAB which was used for ZnS/MMT nanocomposites synthesis and whose presence was proved by the determined carbon content by using AAS and elemental analysis. It was reported that the specific surface area of MMT can diminish due to the plugging of MMT porous structure by CTAB up to ~ 4.4 m²/g [51]. This indicates that further strongly decreased specific surface area of the 4.2 wt.% ZnS/MMT nanocomposite (0.9 m²/g) may be a result of the secondary effect—incorporation of ZnS nanoparticles and/or ZnS agglomerates to MMT meso-macroporous structure. This phenomenon corresponds to Fig. 1b where pores with diameter > 13 nm are evidently disappearing with increasing loading of ZnS nanoparticles from 3.1 to 4.2 wt.%.

The XRD measurements were performed in order to reveal the crystal structure of ZnS nanoparticles and to determine the inter-planar distance of 001 planes (d_{001}) of MMT. The diffraction

Table 1
Textural and optical properties of investigated ZnS/MMT nanocomposites.

Photocatalyst	Nitrogen physisorption		UV-vis
	S_{BET} (m ² /g)	V_{net} (mm ³ liq/g)	Absorption edge (eV)
MMT	28	31	4.02
2.0 wt.% ZnS/MMT	19	40	3.65
3.1 wt.% ZnS/MMT	6.5	22	3.73
4.2 wt.% ZnS/MMT	0.9	3.5	3.84

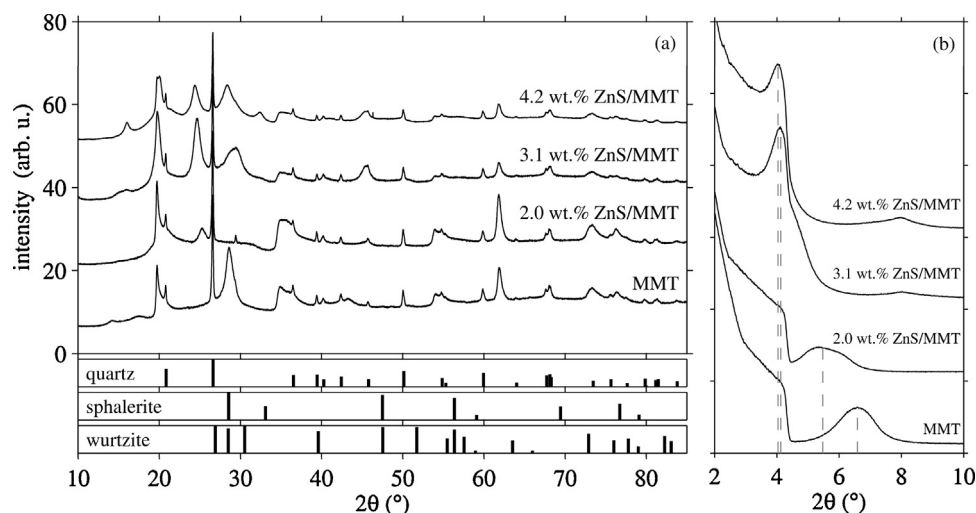


Fig. 2. The diffraction patterns of ZnS/MMT nanocomposites. (a) The positions of the diffraction peaks of individual phases are indicated by black lines below. The height of lines corresponds to the relative intensity of the peaks in logarithmic scale. (b) A detail of the peaks corresponding to 001 planes in MMT. The dashed grey lines indicate the peak positions.

patterns for all the samples including pristine MMT are displayed in Fig. 2a. While the presence of crystalline quartz (trigonal SiO_2 , space group $P3_221$) can be clearly seen, ZnS in any common crystalline form (sphalerite—cubic, $F4_3^-3m$; wurtzite—hexagonal, $P6_3mc$) cannot be proved. This observation might be caused either by very small ZnS crystallite size or due to small amounts of ZnS nanoparticles (2–4.2 wt.%) in the ZnS/MMT nanocomposites since possible ZnS peaks may coincide with those coming from MMT or quartz.

The diffraction maxima corresponding to d_{001} planes in MMT are displayed in detail in Fig. 2b for all the samples. A shift of the 001 diffraction peaks corresponding to an increase of the inter-planar distance d_{001} with increasing concentration of ZnS can be observed (Table 2). This effect can be explained by the presence of some carbon amounts (12–25 wt.%) in all the ZnS/MMT nanocomposites, which come from CTAB used during the deposition of ZnS nanoparticles and is intercalated in the MMT interlayer and thus increases the d_{001} distance of MMT. This feature also pretty correlates with the decreasing specific surface area of investigated nanocomposites in the order 2.0 wt.% ZnS/MMT > 3.1 wt.% ZnS/MMT > 4.2 wt.% ZnS/MMT as a consequence of increasing carbon amounts 12, 19.4 and 25 wt.%, respectively. However, from Table 2 and Fig. 3 is evident that the change in the inter-planar distance d_{001} of MMT at 3.1 wt.% and 4.2 wt.% ZnS loadings is not so substantial despite the significantly increased carbon amount (19.4 and 25 wt.%, respectively). It reveals that at 4.2 wt.% of deposited ZnS the effect of CTAB intercalation to the MMT interlayer is comparable to that for 3.1 wt.% of ZnS and thus the significantly decreased specific surface area of 4.2 wt.% ZnS/MMT nanocomposite ($0.9 \text{ m}^2/\text{g}$) can be caused by plugging of MMT mesopores and macropores by additional CTAB as well as ZnS nanoparticles or their agglomerates, e.g. in the pore mouths. The observations from XRD pretty support the observations from nitrogen physisorption.

Table 2

The position of the 001 diffraction peak in MMT and corresponding inter-planar distances d_{001} with estimated errors.

Photocatalyst	$2\theta_{001}$ (°)	d_{001} (nm)
MMT	6.59 ± 0.02	1.34 ± 0.01
2.0 wt.% ZnS/MMT	5.48 ± 0.04	1.61 ± 0.02
3.1 wt.% ZnS/MMT	4.13 ± 0.02	2.14 ± 0.01
4.2 wt.% ZnS/MMT	4.04 ± 0.02	2.19 ± 0.01

Arising from previous knowledge about possible agglomeration of ZnS nanoparticles stabilized by CTAB [52] and in order to support hypotheses about plugging of MMT porous structure also by ZnS nanoparticles/agglomerates, the TEM analysis of ZnS/MMT nanocomposites was performed as well. The TEM micrographs showing ZnS agglomerates of different sizes deposited on the external surface of MMT are shown in Fig. 4a and b. A detailed view of one ZnS agglomerate revealed that the agglomerates were composed of individual ZnS nanoparticles with sizes of about 20–40 nm. It is in contrast with determined gap energies (see below) corresponding to sizes equal and smaller than 10 nm when the quantum size effect occurs. This apparent disagreement indicates that ZnS nanoparticles of different sizes as well as agglomerated in large agglomerates with sizes of several hundred nanometers exist on MMT. Formation of agglomerates is key for understanding different photocatalytic efficiency discussed below.

Since the same ZnS suspension was used for the preparation of all ZnS/MMT nanocomposites, the size of ZnS nanoparticles does not determine the differences between them. As reported in our previous study [28], ZnS nanoparticles and CTAB form agglomerates attached.

The mean size of ZnS nanoparticles was estimated from their optical properties in a suspension, i.e. before they were deposited on MMT. The well described size-dependence of absorption spectra was considered and the effective mass approximation was utilized

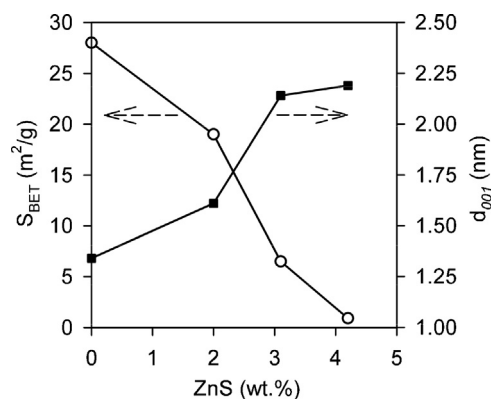


Fig. 3. Correlation between the ZnS loading in MMT, the inter-planar distance of 001 planes (d_{001}) of MMT and the specific surface area of nanocomposites.

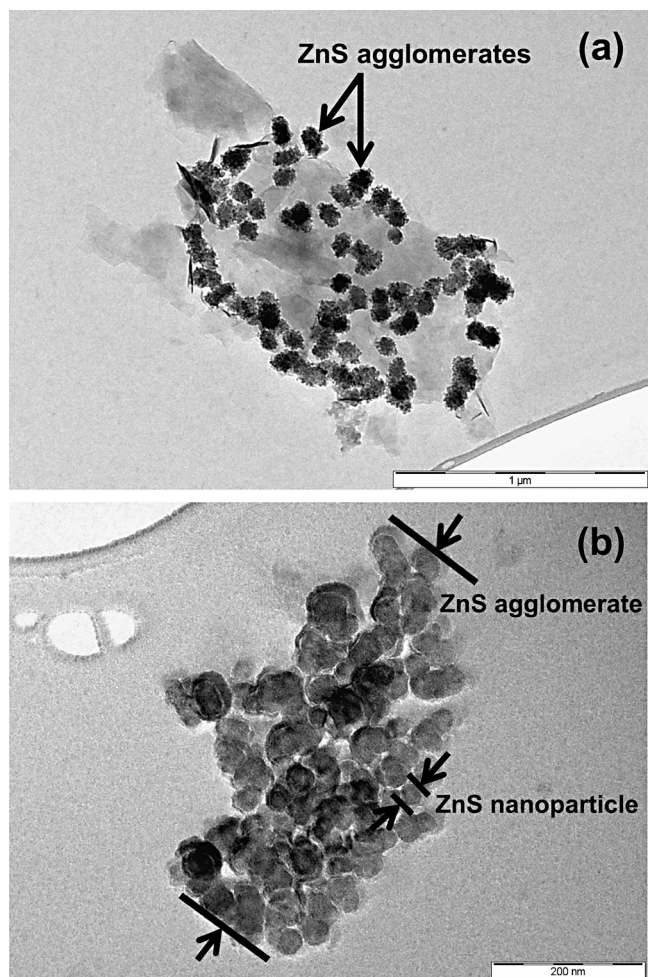


Fig. 4. TEM micrograph of (a) ZnS agglomerates deposited on MMT, (b) detail view on one ZnS agglomerate.

to obtain the size of ZnS nanoparticles from the following Brus equation [53]:

$$E_{\text{bg}}(\text{nano}) - E_{\text{bg}}(\text{bulk}) = \frac{h^2}{8R^2} \left(\frac{1}{m_e^*} + \frac{1}{m_h^*} \right) - \left(\frac{1.8}{\epsilon R} \frac{e^2}{\epsilon R} \right)$$

where $E_{\text{bg}}(\text{bulk})$ and $E_{\text{bg}}(\text{nano})$ are the band gap energies of bulk and nano-sized semiconductors, respectively, h is the Planck constant, m_e and m_h are the effective masses of electron and hole, respectively, and ϵ is the dielectric constant of the material. Here, $m_e = 0.42 m_0$ and $m_h = 0.61 m_0$, where m_0 is the free electron mass and the dielectric constant $\epsilon = 8.76$ [54]. The band gap energy of ZnS nanoparticles was estimated from the linear part of the $(\epsilon h\nu)^{0.5}$ versus $(h\nu)$ plot as described in our previous work [28].

Fig. 5 shows the UV–vis spectra of ZnS/MMT nanocomposites. The band gap energy of ZnS/MMT with 2.0 wt.% of ZnS was 3.65 eV (Table 1). This value is close to that band gap energy reported for bulk ZnS (3.6–3.7 eV) [55]. The band gap energy of ZnS/MMT increased with increasing concentration of ZnS up to 3.84 eV for 4.2 wt.% ZnS/MMT. Previously, it has been reported that the increase in band gap energy is a result of reduction in the particle size of ZnS that is related to the quantum confinement effects [56–58]. The absorption spectra were used to estimate the size of ZnS particles ($2R$) by using of Brus equation: $E_{\text{g}}(R) = E_0 + h^2/(8R^2) \times (1/m_e^* + 1/m_h^*) - 1.8e^2/4\pi\epsilon_0\epsilon R$, where $E_{\text{g}}(R)$ is the energy gap of nanocrystals with radius R , E_0 is the bulk energy gap (3.6 eV), m_e^* and m_h^* are the effective mass of electrons ($0.34 m_e$) and holes ($0.23 m_e$), ϵ_0 is the permittivity of

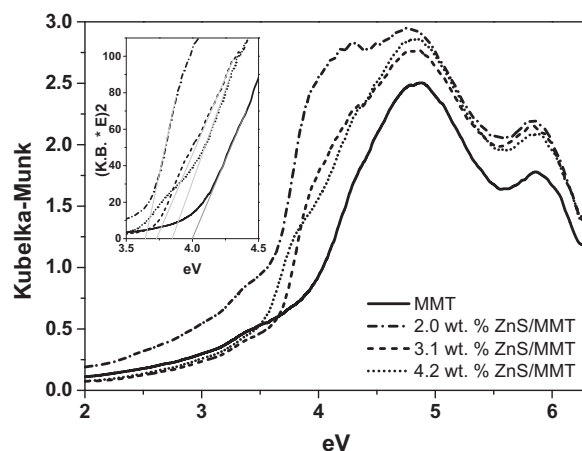


Fig. 5. UV–vis DRS spectra of investigated photocatalysts.

a vacuum, ϵ is the dielectric constant for the ZnS (8.76), h is the Planck constant and e is the charge of an electron. Diameter ($2R$) of studied materials has been estimated to be 10.0 nm, 7.2 nm and 5.7 nm for ZnS/MMT with 2.0 wt.%, 3.1 wt.% and 4.2 wt.% of ZnS. The absolute values of ZnS particles calculated from UV–vis are affected by used E_0 value that has been reported to be 3.6–3.7 eV and the dielectric constant for the ZnS. This is probably a reason, why the absolute value of ZnS particles calculated from UV–vis is lower than those values determined from TEM. Nevertheless, it brings attractive connection between TEM and UV–vis results. It is surprising that the particle diameter of ZnS calculated from the band gap energy (Table 1) decreases with increasing ZnS loading. Moreover, it is in contrast to TEM results. This effect can be explained by clustering of ZnS particles with approximately of the same nano-size. While 2.0 wt.% ZnS/MMT contains separated ZnS nanoparticles with approximately the same diameter of 20–40 nm (TEM—Fig. 4a), 4.2 wt.% ZnS/MMT contains both ZnS nanoparticles and ZnS agglomerates of micrometer-size composed of many of ZnS nanoparticles (TEM—Fig. 4b). Based on that fact the decrease in the band gap energy can be associated with the dominant effect of the presence of higher amount of ZnS nanoparticles and lower amount of ZnS agglomerates.

3.2. Photocatalytic reduction of carbon dioxide

ZnS/MMT nanocomposites with different contents of ZnS were investigated for the photoreduction of CO_2 dissolved in NaOH solutions. The commercial TiO_2 Evonic P25 photocatalyst was examined as a reference for comparison. The effect of irradiation time on the formation of products was investigated over a period of 0–24 h. Fig. 6 shows the evolution of all reaction products as the functions of the irradiation for the 3.1 wt.% ZnS/MMT nanocomposite. The main gaseous product was methane. Hydrogen and low amounts of carbon monoxide were also detected. Other products such as formic acid, formaldehyde, ethane and ethylene could also be formed [22,59], but they were undetectable in our GC configuration. The observed yields ($\mu\text{mol/g}_{\text{cat}}$) order was: $\text{H}_2 > \text{CH}_4 > \text{CO}$.

Comparisons of CH_4 , H_2 and CO yields over ZnS/MMT with different contents of ZnS are shown in Fig. 7a–c, respectively. A gradual increase of methane yield was observed after the start of irradiation with the exception of commercial TiO_2 catalyst. In this case the yields of methane were negligible during the first 8 h of irradiation. The highest yield of methane was observed for 3.1 wt.% ZnS/MMT.

In case of ZnS/MMT, the hydrogen yields continually increased during the whole experiments. In comparison with the application

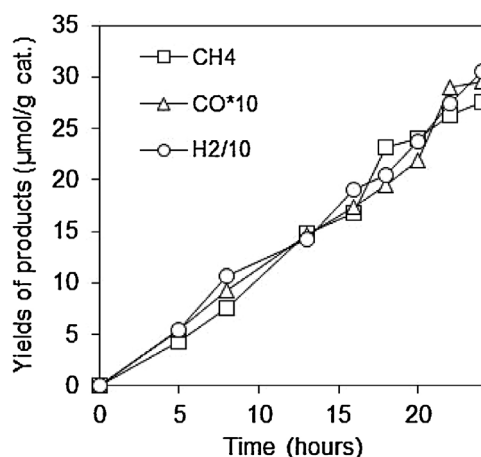


Fig. 6. Time dependence of the product concentrations over the 3.1 wt.% ZnS/MMT nanocomposite.

of commercial titanium dioxide, hydrogen was produced in 6-fold higher concentrations (Fig. 7b). The yields of carbon monoxide were increasing slowly during the reaction, but all yields were close to the limit of detection (Fig. 7c). The highest yield of both products was observed for 3.1 wt.% ZnS/MMT.

The data from the longest reaction time span were chosen for the overall comparison because the yields of all products were the highest and the most accurate. The results show that the photocatalytic performance of nanocomposites varies with the content of ZnS in the order of 3.1 wt.% ZnS > 4.2 wt.% ZnS > 2.0 wt.% ZnS. All yields of products for ZnS/MMT nanocomposites were higher than those for the commercial photocatalyst Evonic P25. According to the blank test, the original montmorillonite does not possess any photocatalytic performance.

Regarding the possible formation of reaction products in a consequence of some carbon content from CTAB presented, it is worth to mention that the formation of methane was already investigated with the developed type of nanocomposite within the blank experiments at various pH in our previous study [60]. The generation of methane was observed, the effect of different pH on the methane yields was comparable. However, in our study the evolution of photocatalytic performance of ZnS/MMT nanocomposites does not follow the trend in increasing carbon content (within increasing ZnS loading), thus the determined trend in photocatalytic performance can be considered as not burdened with this fact and correct.

4. Discussion

One would assume that with increasing loading of ZnS nanoparticles, which is the only active component in the ZnS/MMT nanocomposites, the photocatalytic performance of investigated nanocomposites would escalate. However, this hypothesis was not confirmed. According to the blank test, the original montmorillonite does not possess any photocatalytic performance. Besides that, 4.2 wt.% of ZnS on MMT does not assign the highest photocatalytic performance. The overall order of photocatalytic performance in the photocatalytic reduction of CO₂ was following: 3.1 wt.% ZnS > 4.2 wt.% ZnS > 2.0 wt.% ZnS. It is evident that with higher content of ZnS the nanocomposite photocatalytic performance in the first instance increases, but then there is a decline. This indicates that probably besides the ZnS loading, also the degree of agglomeration of ZnS nanoparticles plays a key role. The agglomeration of ZnS nanoparticles increases with increasing ZnS loading as it is evident from the results of TEM and UV-vis and it could be correlated with the work function as follows. The work

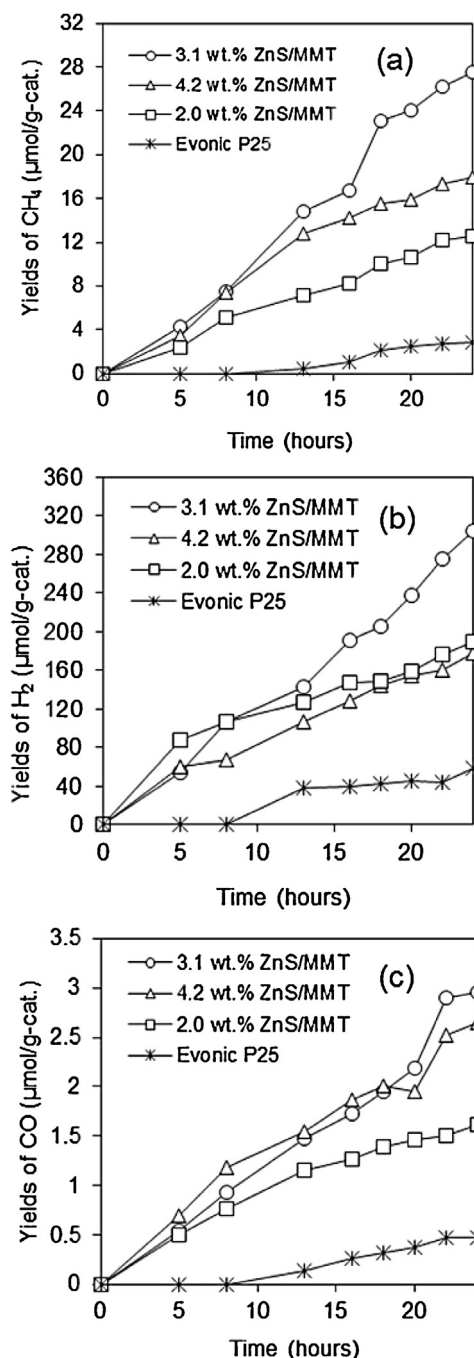


Fig. 7. Time dependence of (a) methane, (b) hydrogen and (c) carbon monoxide yields over the ZnS/MMT nanocomposites with different content of ZnS and commercial TiO₂ catalysts (Evonic P25).

function is the minimum energy that must be given to an electron to liberate it from the surface of ZnS nanoparticle. If ZnS occurs on MMT as same-size nanoparticles in various ZnS loadings, the work function should be same. We suppose, if such ZnS nanoparticles agglomerate and the degree of their agglomeration is too high, the work function should be higher. In our case with increasing ZnS loading the nanoparticles agglomerate and the lowest work function is achieved for 3.1 wt.% of ZnS in MMT, when ZnS is partially as separated nanoparticles and partially as agglomerates. This evidences the correlation between the degree of ZnS nanoparticles agglomeration and the work function.

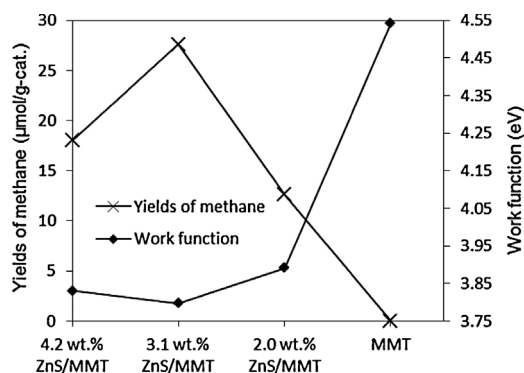


Fig. 8. Correlation between the work function and the photocatalytic performance of investigated photocatalysts.

Fig. 8 shows the correlation between the yields of methane after 24 h of irradiation and the work function of each catalyst. It can be seen from Fig. 8 that the lowest electron work function corresponds to the most active catalyst. This observation is in agreement with our previous observations over cerium doped TiO_2 nanoparticulated photocatalysts in the same reaction [61] and corresponds to the reaction mechanism. The photocatalytic reduction of carbon dioxide is conducted via generated electrons and the 3.1 wt.% ZnS/MMT nanocomposite releases those electrons most easily. Contrary to that, pristine montmorillonite shows no photocatalytic performance, corresponding nicely to very high electron work function.

The valence band of sulfide semiconductors, made of 3p orbitals of the sulfur atoms, is shifted upwards compared with those of the oxide analogues, while the conduction band electrons are also more reductive [62]. For the CO_2 photocatalytic reduction the electron energy in conduction band must be higher than H^+ reduction potential and the hole energy in valence band must be lower than OH^- oxidation potentials. ZnS is a direct wide

band gap semiconductor ($E_g = 3.6 \text{ eV}$ in the bulk) [63], hence it absorbs only in the UV range, but it possesses a strongly reducing conduction band ($E_{\text{CB}} = -1.85 \text{ V}$ versus the NHE at pH 7) [64]. The addition of ZnS to MMT should result in changing the band gap and the absorption edge energies can be expected and was also experimentally demonstrated (see Fig. 5). However, it is always difficult to predict separately the shift of conduction and valence band energies, which are extremely important with respect to required oxidation and reduction potentials.

The work function for different ZnS contents shown in Fig. 8 can help us to elucidate the shifts of conduction as well as valence bands. For simplicity the Fermi level on nanoparticle surface is supposed to be pinned to the middle of the nanoparticle band gap. Deriving from Figs. 5 and 8 and Table 1, we can estimate that the energy of electrons on the conduction band edge is -2.066 eV , while the valence band edge is -5.716 eV for 2.0 wt.% ZnS/MMT (Fig. 9a). For 3.1 wt.% ZnS/MMT the energy of electrons on the conduction band edge increases about approximately 134 meV, while the valence band edge shifts up by 54 meV. Further increase of ZnS content up to 4.2 wt.% led only to a much smaller conduction band decrease (21 meV), whereas the valence band edge shifts down by 89 meV. These shifts are depicted in Fig. 9b. Higher levels of the conduction band are more effective for the creation of H^+ ions which are necessary for CO_2 reduction. It can be concluded that for 3.1 wt.% of ZnS the carriers have the most suitable potentials for the photocatalytic reduction of CO_2 .

In summary: Since the optical and electronic properties of nanocomposites have been considered as key properties related to the mechanism of CO_2 photocatalytic reduction and there exist the correlation between the band gap energy, the nanoparticle work function and the degree of agglomeration of nanoparticles, the behavior of ZnS on nano-size level plays the determining role. The shift in conduction band and valence band energies of ZnS at different ZnS loadings is a consequence of different degree of ZnS nanoparticles agglomeration on MMT.

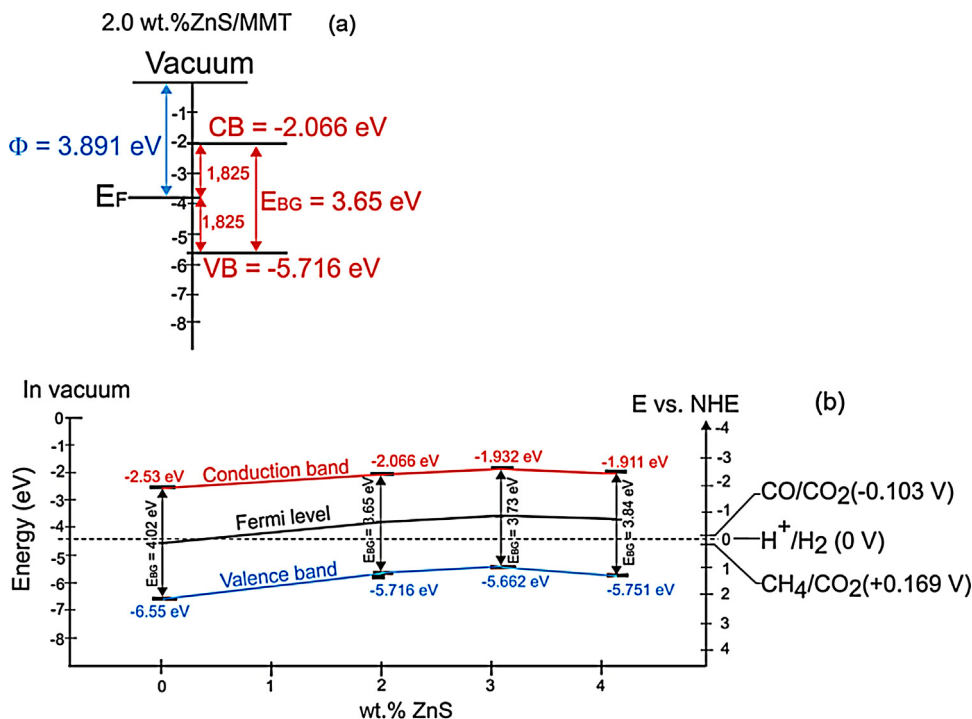


Fig. 9. Illustration of (a) the evaluation of energies of electrons and holes in conduction and valence bands from the knowledge of experimentally determined work function and band gap energy for the 2.0 wt.% ZnS/MMT nanocomposite and (b) the shifts of energies of electrons and holes in conduction and valence bands in dependence on the ZnS loading.

5. Conclusions

ZnS nanoparticles stabilized by cetyltrimethylammonium bromide were deposited on montmorillonite (MMT) forming the ZnS/MMT nanocomposites with ZnS loadings within 2.0–4.2 wt.%. The key role in the performance of ZnS/MMT nanocomposites in the CO₂ photocatalytic reduction played the energies of electrons and holes within the electronic structure of designed photocatalytic materials, which were in fact affected by ZnS loadings. The potentials of electrons and holes required for the photocatalytic reduction of CO₂ were the most suitable for the 3.1 wt.% ZnS/MMT nanocomposite. All prepared ZnS/MMT nanocomposites exhibited higher efficiency in the photocatalytic CO₂ reduction in comparison with the commercial TiO₂ Evonic P25.

Acknowledgments

The financial support of the EU project No. CZ.1.05/2.1.00/03.0069 “ENET”, the Grant Agency of The Czech Republic (project No. 14-35327J) and “National Feasibility Program I”, project LO1208 “TEWEP” from Ministry of Education, Youth and Sports of the Czech Republic is gratefully acknowledged. Lenka Matějová acknowledges the support in the framework of the project “Opportunity for young researchers”, reg. No. CZ.1.07/2.3.00/30.0016, supported by Operational Programme Education for Competitiveness and co-financed by the European Social Fund and the state budget of the Czech Republic.

References

- [1] R. Richter, S. Caillol, J. Photochem. Photobiol., C: Photochem. Rev. 12 (2011) 1–19.
- [2] S.N. Habisreutinger, L. Schmidt-Mende, J.K. Stolarczyk, Angew. Chem. Int. Ed. 52 (2013) 7372–7408.
- [3] H. Yoneyama, Catal. Today 39 (1997) 169–175.
- [4] H. Fujiwara, H. Hosokawa, K. Murakoshi, Y. Wada, S. Yanagida, J. Phys. Chem. B 101 (1997) 8270–8278.
- [5] P. Johne, H. Kirsch, J. Photochem. Photobiol., A: Chem. 111 (1997) 223–228.
- [6] B.-J. Liu, T. Torimoto, H. Yoneyama, J. Photochem. Photobiol., A: Chem. 113 (1998) 93–97.
- [7] P. Praus, O. Kozák, K. Kočí, A. Panáček, R. Dvorský, J. Colloid Interface Sci. 360 (2011) 574–579.
- [8] K. Sayama, H. Arakawa, J. Phys. Chem. 97 (1993) 531–533.
- [9] Y. Kohno, T. Tanaka, T. Funabiki, S. Yoshida, Chem. Commun. 9 (1997) 841–842.
- [10] Y. Kohno, T. Tanaka, T. Funabiki, S. Yoshida, J. Chem. Soc., Faraday Trans. 94 (1998) 1875–1880.
- [11] Y. Kohno, T. Tanaka, T. Funabiki, S. Yoshida, Phys. Chem. Chem. Phys. 2 (2000) 2635–2639.
- [12] Y. Kohno, T. Tanaka, T. Funabiki, S. Yoshida, Phys. Chem. Chem. Phys. 2 (2000) 5302–5307.
- [13] S. Yoshida, Y. Kohno, Catal. Surv. Jpn. 4 (2001) 107–114.
- [14] Y. Kohno, H. Ishikawa, T. Tanaka, T. Funabiki, S. Yoshida, Phys. Chem. Chem. Phys. 3 (2001) 1108–1113.
- [15] K. Teremura, T. Tanaka, H. Ishikawa, Y. Kohno, T. Funabiki, J. Phys. Chem. B 108 (2004) 346–354.
- [16] N. Gokon, N. Hasegawa, H. Kaneko, H. Aoki, Y. Tamaura, M. Kitamura, Sol. Energy Mater. Sol. Cells 80 (2003) 335–341.
- [17] I.-H. Tseng, W.-C. Cheng, J.C.S. Wu, Appl. Catal., B: Environ. 37 (2002) 37–48.
- [18] I.-H. Tseng, J.C.S. Wu, H.-Y. Chou, J. Catal. 221 (2004) 432–440.
- [19] G.R. Dey, A.D. Belapurkar, K. Kishore, J. Photochem. Photobiol., A: Chem. 163 (2004) 503–508.
- [20] J.C.S. Wu, H.-M. Lin, C.-L. Lai, Appl. Catal., A: Gen. 296 (2005) 194–200.
- [21] Slamet, H.W. Nasution, E. Purnama, S. Kosela, J. Gunlazuardi, Catal. Commun. 6 (2005) 313–319.
- [22] N. Sasirekha, S.J.S. Basha, K. Shanthi, Appl. Catal., B: Environ. 62 (2006) 169–180.
- [23] S.S. Tan, L. Zou, E. Hu, Catal. Today 115 (2006) 269–273.
- [24] S.S. Tan, L. Zou, E. Hu, Sci. Tech. Adv. Mater. 8 (2007) 89–92.
- [25] X.-H. Xia, Z.-J. Jia, Y. Yu, Y. Liang, Z. Wang, L.-L. Ma, Carbon 45 (2007) 717–721.
- [26] S. Liu, Z. Zhao, Z. Wang, Photochem. Photobiol. Sci. 6 (2007) 695–700.
- [27] C.-C. Lo, C.-H. Hung, C.-S. Yuan, J.-F. Wu, Sol. Energy Mater. Sol. Cells 91 (2007) 1765–1774.
- [28] O. Kozák, P. Praus, K. Kočí, M. Klementová, J. Colloid Interface Sci. 352 (2010) 244–251.
- [29] X.V. Zhang, S.P. Ellery, C.M. Friend, H.D. Holland, F.M. Michel, M.A.A. Schoonen, S.T. Martin, J. Photochem. Photobiol., A: Chem. 185 (2007) 301–311.
- [30] I. Fatimah, S. Wang, K. Wijaya, Appl. Clay Sci. 50 (2010) 588–593.
- [31] I. Fatimah, S. Wang, D. Wulandari, Appl. Clay Sci. 53 (2011) 553–560.
- [32] Y. Li, J.R. Liu, S.Y. Jia, J.W. Guo, J. Zhuo, P. Na, Chem. Eng. J. 191 (2012) 66–74.
- [33] J. Li, F. Wu, G. Mailhot, N. Deng, J. Hazard. Mater. 174 (2010) 368–374.
- [34] M. Tahir, N.S. Amin, Appl. Catal., B: Environ. 142–143 (2013) 512–522.
- [35] K. Chen, J. Li, W. Wang, Y. Zhang, X. Wang, H. Su, Appl. Surf. Sci. 257 (2011) 7276–7285.
- [36] J. Liu, M. Dong, S. Zuo, Y. Yu, Appl. Clay Sci. 43 (2009) 156–159.
- [37] X. Zhao, X. Quan, S. Chen, H. Zhao, Y. Liu, J. Environ. Sci. 19 (2007) 358–361.
- [38] S.-Z. Kang, T. Wu, X. Li, J. Mu, Desalination 262 (2010) 147–151.
- [39] H. Boukhatef, L. Djouadi, N. Abdelaziz, H. Khalaf, Appl. Clay Sci. 72 (2013) 44–48.
- [40] R. Kun, K. Mogorósi, I. Dékány, Appl. Clay Sci. 32 (2006) 99–110.
- [41] Czechoslovakia State Standard, ČSN 720101, Basic analysis of Silicates—Decomposition, Institute for Normalization and Measurement, Prague, 1974.
- [42] S. Brunauer, P.H. Emmett, E. Teller, Adsorption of gases in multi-molecular layers, J. Am. Chem. Soc. 60 (1938) 309–319.
- [43] S.J. Gregg, K.S.W. Sing, Adsorption. Surface Area and Porosity, Academic Press, New York, NY, 1982.
- [44] J.B. DeBoer, B.C. Lippens, B.G. Linsen, J.C.P. Broekhoff, A.V.D. Heuvel, Th.J. Osinga, J. Colloid Interface Sci. 21 (1966) 405–414.
- [45] E.P. Barret, L.G. Joyner, P.B. Halenda, J. Am. Chem. Soc. 73 (1951) 373–380.
- [46] J. Tauc, A. Menth, J. Non-Cryst. Solids 569 (1972) 8–10.
- [47] J. Tauc, Amorphous and Liquid Semiconductors, Plenum Press, London, 1974.
- [48] K. Kočí, L. Obalová, D. Plachá, Z. Lacný, Collect. Czech. Chem. Commun. 73 (2008) 1192–1204.
- [49] P. Praus, J. Matys, O. Kozák, J. Braz. Chem. Soc. 23 (2012) 1900–1906.
- [50] R. Dvorský, J. Trojčková, P. Praus, J. Luňáček, Mater. Res. Bull. 48 (2013) 2286–2288.
- [51] P. Praus, M. Turicova, S. Študentova, M. Ritz, J. Colloid Interface Sci. 304 (2006) 29–36.
- [52] P. Praus, R. Dvorský, P. Horínková, M. Pospíšil, P. Kovář, J. Colloid Interface Sci. 377 (2012) 58–63.
- [53] L.E. Brus, J. Chem. Phys. 80 (1984) 4403–4410.
- [54] K. Dutta, S. Manna, S.K. De, Synth. Met. 159 (2009) 315–319.
- [55] K. Sooklal, B.S. Cullum, S.M. Angel, C.J. Murphy, J. Phys. Chem. 100 (1996) 4551–4555.
- [56] R.S.S. Saravanan, D. Pukazhselvan, C.K. Mahadevan, J. Alloys Compd. 517 (2012) 139–146.
- [57] G. Ghosh, M.K. Naskar, A. Patra, M. Chatterjee, Opt. Mater. 28 (2006) 1047–1053.
- [58] S. Nazerdeylami, E. Saievar-Iranizad, Z. Dehghani, M. Molaei, Physica B: Condens. Matter 406 (2011) 108–111.
- [59] K. Adachi, K. Ohta, M. Mizuno, Sol. Energy 53 (1994) 187–190.
- [60] P. Praus, M. Reli, K. Kočí, L. Obalová, Appl. Surf. Sci. 275 (2013) 369–373.
- [61] L. Matějová, K. Kočí, M. Reli, L. Čapek, A. Hospodková, P. Peikertová, Z. Matěj, L. Obalová, A. Wach, P. Kuśtrowski, A. Kotarba, Appl. Catal., B: Environ. 152–153 (2014) 172–183.
- [62] K. Maeda, K. Domen, J. Phys. Chem. C 111 (2007) 7851–7861.
- [63] D.S. Bhattachande, V.G. Pangarkar, A.A.C.M. Beenackers, J. Chem. Technol. Biotechnol. 77 (2002) 102–116.
- [64] F.R.F. Fan, P. Leempoel, A.J. Bard, J. Electrochem. Soc. 130 (1983) 1866–1875.